aerospace

Article

Modeling and Analysis of Staged Constellation Deployment from a Single-Unit System

Daniel Cumbo * and Marc Anthony Azzopardi

Department of Electronic Systems Engineering, University of Malta, MSD2080 Msida, Malta; marc.azzopardi@um.edu.mt
* Correspondence: daniel.cumbo.12@um.edu.mt

Abstract

A novel satellite architecture and deployment method is proposed to reduce the logistical cost and complexity of launching and dispersing satellite constellations. The architecture consists of a primary satellite that separates into multiple smaller units, which are subsequently dispersed using differential drag. An algorithm is developed to determine the required disengagement velocities and optimal timing for separation maneuvers. Two case studies with orbital simulations demonstrate the feasibility of this approach for constellation deployment and phasing. The results indicate that while mission-specific factors influence deployment dynamics, informed selection of the disengagement velocities is crucial for minimizing phase times and mitigating potential delays. The findings confirm the feasibility of the proposed architecture and dispersal method, offering a cost-effective alternative to traditional deployment strategies for future satellite constellations.

Keywords: constellation formation; formation keeping; differential drag control; relative orbit control algorithm; constellation deployment

Academic Editors: Fanghua Jiang and M. Reza Emami

Received: 16 May 2025
Revised: 12 June 2025
Accepted: 27 June 2025
Published: 29 June 2025

Citation: Cumbo, D.; Azzopardi, M.A. Modeling and Analysis of Staged Constellation Deployment from a Single-Unit System. *Aerospace* **2025**, *12*, 586. https://doi.org/10.3390/aerospace12070586

1. Introduction

Satellite constellations have traditionally been deployed through multiple launches, either releasing one satellite at a time or dedicating each launch to a specific orbital plane [1]. For pico- and nano-satellites, this approach presents additional challenges due to dependence on rideshare opportunities, which restrict control over launch timing and orbit insertion [2]. A notable example is the PlanetScope constellation of 130 3U CubeSats, which required deployment via multiple launch vehicles, including Falcon 9, Electron, and PSLV [3]. Although widely adopted due to the lack of practical alternatives, this deployment strategy is costly, logistically demanding, and complicates financial planning because of fluctuating prices between launches.

Moreover, rideshare missions struggle to synchronize orbital plane insertions, leading to orbital misalignments that necessitate post-deployment corrections, leading to prolonged phase times unless propulsion is available [1], a limitation compounded by the fact that propulsion is often impractical for mass- and volume-constrained satellites [4]. To overcome these limitations, we propose a single-launch deployment strategy, where multiple satellites are assembled into a single unit that separates in orbit through a staged disengagement sequence. Each disengagement introduces a controlled change in velocity, or Δv, which is enhanced via differential drag control to phase the constellation. The approach reduces launch scheduling complexity, eliminates multi-launch coordination, and enables scalable deployments in low-Earth orbit (LEO).

Differential drag control is a technique that modulates atmospheric drag via satellite reorientation or deployable surfaces. It allows along-track control for formation flying, constellation phasing, and collision avoidance. Demonstrated by various missions such as Planet Labs' Flock, CYGNSS, AeroCube-4, and ORBCOMM [5–8], it has become a standard method for managing relative satellite motion. More recently, Joen et al. demonstrated its applicability to periodic rendezvous missions in their design of a coronagraph consisting of two CubeSats [9].

Advanced control strategies for differential drag include linear programming [10], LQR- and Lyapunov-based adaptive methods [11], convex optimization [12], and hybrid schemes combining drag with limited propulsion or lift modulation [13–15]. These strategies explore centralized and decentralized architectures, some leveraging inter-satellite communication and nodal precession for limited cross-track control.

Differential drag control also has its limitations. Particularly, its effectiveness depends on altitude and atmospheric density, which varies with solar activity [6]. Phasing is inherently slower than thruster-based methods, often requiring weeks to months, and is largely restricted to in-plane maneuvers. Additionally, it relies on limited drag-state resolution and pointing accuracy [12]. Nonetheless, it remains an attractive option for satellites without onboard propulsion, offering a viable means of achieving relative positioning using only attitude control.

Despite being developed using a variety of methods, existing differential drag control strategies generally assume that the initial relative positions and velocities are solely determined by the deployment conditions imposed by the launch vehicle. In contrast, the proposed deployment method provides additional control over the initial relative orbital parameters by leveraging its disengagement mechanics. Therefore, the novelty of this work lies not only in the proposed deployment architecture and dispersal strategy but also in the extension of existing research to make such a framework feasible. In particular, this work builds upon Planet Labs' model in [5] to provide an algorithm that selects the disengagement Δv magnitude and timing range to determine phase times.

The contribution of this work lies in the novel deployment method proposed, wherein multiple satellites are launched as a single integrated unit and subsequently disengaged and dispersed in a hierarchical manner. This is accompanied by the development of generalized algorithms for constellation phasing, which determine the phase times, required Δv values, and corresponding disengagement timings to achieve the desired orbital spacing of constellations deployed from the many-in-one configuration.

Following this introduction, the paper is divided into three main sections. The first section defines the problem through a set of assumptions and outlines the nomenclature and conventions adopted throughout the work. It also introduces the disengagement and phasing equations, which are adapted for the proposed deployment method and used to assess its effectiveness. The second section presents the methodology, detailing the algorithms developed for an enumerative simulation of the deployment process. The third section provides two case studies, one for PocketQube-class satellites and another for CubeSat-class satellites, in which the disengagement sequence is evaluated under the influence of attitude control inaccuracies. The paper concludes with a discussion of the proposed methodology, including a comparison with the Planet Labs deployment model and an assessment of the approach's advantages and limitations.

2. Defining the Deployment Problem

The dispersal problem is defined in the context of deploying a many-in-one satellite system, where a constellation is launched as a single unit and sequentially separates until full deployment. This formulation imposes no restrictions on satellite size or quantity but operates under the following assumptions:

1. Satellites are cube-shaped;
2. Satellites are identical in terms of external surface properties, mass, and shape;
3. Constellation orbit is circular or quasi-circular;
4. Constellation size follows 2^x, where x is a positive real integer;
5. No onboard propulsion;
6. All satellites have three-axis attitude control capabilities.

The first three assumptions ensure scalability across different constellation sizes while maintaining predictable dispersal behavior. The fourth assumption standardizes disengagement parameters across all deployment stages. The fifth assumption is not intended to limit applicability but rather to establish a baseline case from which the efficacy of passive control methods can be evaluated. The final is a necessity, as it is central to the concept of differential drag control, with active attitude control required throughout the mission. This is also required for detumbling and pointing during disengagement.

Additionally, this study focuses on satellite constellations deployed at initial orbital altitudes of up to 600 km, beyond which the decreasing atmospheric density significantly limits the effectiveness of differential drag-based dispersal. For the analysis presented here, only eccentricities up to 0.01 are considered. Higher eccentricities introduce greater modeling challenges for differential drag control for two main reasons. First, the substantial variation in atmospheric density between periapsis and apoapsis complicates the modeling of available control authority. Second, maintaining relative angular configurations becomes more difficult due to orbit perturbations associated with higher eccentricities, particularly the precession of the argument of perigee.

2.1. Notation and Convention

To ensure clarity and consistency, standardized notation is used throughout the analysis. The indexing and numbering of satellites and their parameters within the constellation are summarized in Table 1.

Table 1. Dispersal notations and descriptions.

Symbol	Description
k	Deployment stage index $(k = 0,\ 1,\ \ldots,\ k_{max})$
n	Total number of satellites, $n = 2^x$ with $x \in N$
$S_{k,0}$	Reference satellite at stage k
$S_{k,i}$	ith satellite at stage k from $S_{k,0}$ by proximity
$\theta_{k,i}$	Angular separation between $S_{k,i}$ and $S_{k,0}$

Deployment Stages: Stages are indexed by k, where $k = 0$ at initial deployment when all satellites are combined as a single unit. The current stage increments following the disengagement maneuver of satellites in the previous stage. Full deployment is reached at $k = k_{max}$, where $k_{max} = \log_2 n$, and n is the total number of satellites.

Satellite Indexing: At each stage k, one satellite is designated as the reference satellite, denoted $S_{k,0}$. The remaining satellites are indexed based on their initial proximity to the reference satellite: $S_{k,1},\ S_{k,2} \ldots\ S_{k,m}$, where $m = 2^k - 1$. By convention, the reference satellite begins in low-drag mode, while the rest begin in high-drag mode.

Angular Separation: Differential drag control is based on angular separation dynamics. The relative position of each satellite in a given stage is defined by its angular separation $\theta_{k,i}$ from the reference satellite $S_{k,0}$, where $i = 1,\ 2,\ \ldots,\ m$. The rates of change are denoted by $\dot{\theta}_{k,i}$ (angular velocity) and $\ddot{\theta}_{k,i}$ (angular acceleration).

Disengagement Mechanics: The separation mechanism imparts a differential velocity change (Δv) to the two resulting satellites, with one receiving $+\Delta v$ and the other $-\Delta v$. The satellite experiencing the most consecutive negative Δv instances across stages is designated as the reference. By convention, satellites with odd i values ($i = 1, 3, \ldots$) receive $+\Delta v$, while even-indexed satellites receive $-\Delta v$.

2.2. Disengagement Sequence

Through k_{max} successive separation events at perigee passes, the system transitions from a many-in-one satellite to a fully deployed constellation. At each deployment stage k, every satellite from the previous stage undergoes a disengagement maneuver, increasing the total number of satellites to 2^k until the final configuration of n satellites is reached. Each phase includes controlled phasing via differential drag control for constellation formation. Figure 1 illustrates a three-stage sequence, whilst the disengagement process is outlined as follows:

1. Initial Deployment: The satellite system is deployed as a single unit made up of n satellites.
2. First Disengagement ($k = 1$): Upon reaching the first perigee following the disengagement command, the primary unit undergoes a disengagement maneuver. This process results in the formation of two distinct sub-units.
3. First Sub-Unit Phase: Following the initial disengagement, the two newly formed sub-units undergo a controlled phasing process, gradually achieving a predefined in-plane separation angle.
4. Subsequent Disengagement Sequences ($k = 2, 3, \ldots, k_{max}$): Following the phasing process and at the subsequent perigee pass, each satellite from the previous stage undergoes a disengagement maneuver, progressively increasing the total number of orbiting satellites to 2^k. Following each disengagement, each sub-unit is phased to a predefined in-plane separation angle.
5. Final Disengagement at ($k = k_{max}$): At the last deployment stage, each of the satellites from the previous phase undergoes a final separation, completing the deployment and reaching the total constellation size n.
6. Final Phasing and Constellation Formation: With all n satellites deployed, one is designated as the reference unit, while the remaining $n - 1$ satellites are phased into their final constellation configuration using differential drag control to achieve the desired spatial distribution with respect to the designated reference.

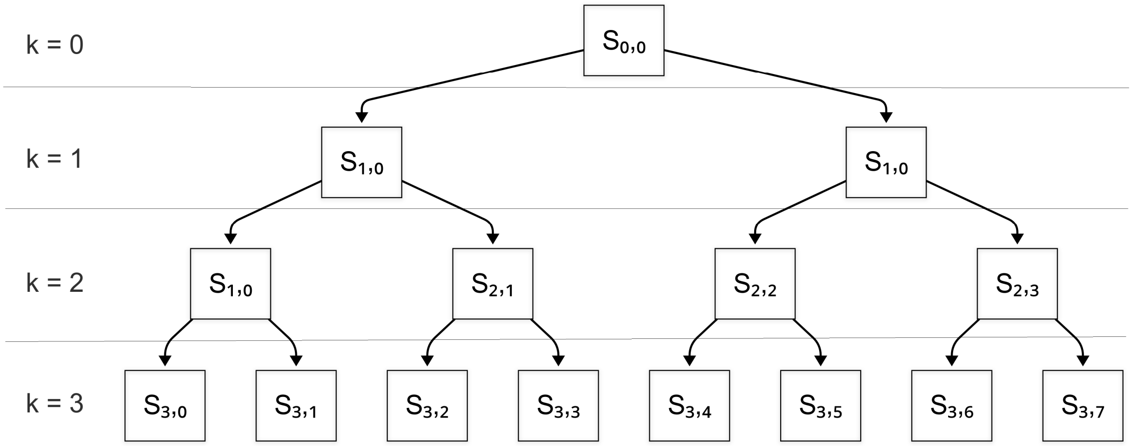

Figure 1. Multi-stage satellite deployment with $k_{max} = 3$.

2.3. The Disengagement Maneuver

As a result, their mean motions also diverge, with the lower satellite orbiting faster, gradually altering the relative angular separation of the satellites. To maximize phasing efficiency, the change in orbital energy ΔE must also be optimized. The change in energy is derived from the vis-viva equation, Equation (1), as:

$$\Delta E = \frac{1}{2}\Delta v^2 + v_0 \Delta v \cos(\alpha) \tag{1}$$

where $\alpha = 0$ represents a tangential disengagement along the velocity vector, and $\alpha = \frac{\pi}{2}$ represents a radial disengagement. Since $v_0\ \Delta v\cos(\alpha)$ is the dominant term, then tangential disengagement at perigee, where v_0 is highest, maximizes energy change. The magnitude of Δv affects phasing times and is incorporated into the optimization algorithm, where it needs to be large enough to sufficiently alter orbital velocity and minimize the risk of post-disengagement collisions while also governing the initial separation rates during phasing. This study focuses, in part, on determining the required Δv magnitude but does not address the disengagement mechanism design.

2.4. Satellite Dispersal and Phasing

The model follows that presented by Planet Labs satellites in [5] for the Dove satellites' in-plane phasing. A discretized set of Cartesian position and velocity vectors of the constellation is converted into separation angles, θ, and their rate of change, $\dot{\theta}$, with respect to a designated reference satellite over a 24 h period, k. The separation angles experience acceleration due to the application of differential drag, with the magnitude given by Equation (2).

$$\ddot{\theta}_k = \frac{3q_{ref,k}}{\overline{a}_{ref}}\left(\frac{1}{\beta_{Min}} - \frac{1}{\beta_{Max}}\right) \tag{2}$$

Here, $\beta = \frac{m}{sc_D}$, $\overline{a}_{ref}$ is the mean semi-major axis of the reference satellite, and $q_{ref,k}$ is the mean dynamic pressure over the discretized period k given by $q_{ref,k} = \frac{1}{2}\overline{\rho v^2}$. This angular acceleration serves as the control variable, providing either acceleration or deceleration between a satellite and reference pair. It is controlled through the attitude determination and control system (ADCS) commands using a binary control scheme, in which the satellites orient themselves to align with either β_{Max} and β_{Min}, corresponding to low-drag and high-drag mode ballistic coefficients, respectively. Effectively, this splits the phasing time of the two satellites into an acceleration period and a deceleration period, denoted by Δt_a and Δt_b. Minimizing the sum of these two periods results in the optimal phasing time.

Foster et al. also provide an analytical solution for the two-satellite phasing problem in [5], which is directly applicable to each satellite–reference pair in this deployment strategy. For a given pair with initial and final states defined by $\left[\theta\ \dot{\theta}\right]_0^T$ and the desired final relative motion $\left[\theta\ \dot{\theta}\right]_f^T$, the optimal switching times are given by Equations (3) and (4):

$$\Delta t_B = \frac{\Delta\dot{\theta} - \ddot{\theta}_A \Delta t_A}{\ddot{\theta}_B} \tag{3}$$

and

$$\left[\frac{1}{2}\ddot{\theta}_A\left(\frac{\ddot{\theta}_A}{\ddot{\theta}_B} - 1\right)\right]\Delta t_A^2 + \left[\dot{\theta}_0\left(\frac{\ddot{\theta}_A}{\ddot{\theta}_B} - 1\right)\right]\Delta t_A + \left[\Delta\theta - \frac{\Delta\dot{\theta}}{\ddot{\theta}_B}\left(\dot{\theta}_0 + \frac{1}{2}\Delta\dot{\theta}\right)\right] = 0 \tag{4}$$

where $\ddot{\theta}_A = \ddot{\theta}$, $\ddot{\theta}_B = -\ddot{\theta}$, $\Delta\theta = \theta_f - \theta_0$, and $\Delta\dot{\theta} = \dot{\theta}_f - \dot{\theta}_0$. The solution is the Δt_a and Δt_b that provide positive, real roots for the given relative motion and angular acceleration.

In a many-in-one system, the total phasing process begins immediately after separation from the launch vehicle at $\mathrm{k} = 0$ and continues through each deployment stage $(\mathrm{k} = 1, 2, \ldots, \mathrm{k}_{\max} - 1)$. Each stage consists of a disengagement maneuver followed by a phasing interval governed by Equations (3) and (4). The phasing duration of each stage is thus determined by the initial and final angular states, which evolve recursively based on the disengagement history and the differential drag control authority.

Starting from Stage 1, the problem consists of two satellites, $S_{1,0}$ and $S_{1,1}$. The reference satellite will enter low-drag mode first, allowing $S_{1,1}$ to accelerate by some value, $\ddot{\theta}_{1,1}$, until $\begin{bmatrix}\theta_{1,1} & \dot{\theta}_{1,1}\end{bmatrix}^T_f$ is reached. At the next perigee pass, both satellites perform a disengagement maneuver, which results in four satellites. This includes $S_{2,2}$ and $S_{2,3}$, which previously formed $S_{1,1}$, as well as $S_{2,0}$ and $S_{2,1}$, which previously formed $S_{1,0}$. This process repeats until the final configuration of n satellites is reached. In the final stage, the drag configuration is no longer defined by convention but instead is determined analytically for each satellite using the phasing equations above.

The disengagement sequence inherently creates multiple branches where the two satellites resulting from a disengagement are coupled through the same initial conditions. For example, in an eight-satellite system, four primary branches emerge:

- Branch 1:
    - $S_{0,0} \rightarrow S_{1,1} \rightarrow S_{2,3} \rightarrow S_{3,6}, S_{3,7}$;
    - $S_{0,0} \rightarrow S_{1,1} \rightarrow S_{2,2} \rightarrow S_{3,4}, S_{3,5}$.
- Branch 2: $S_{0,0} \rightarrow S_{1,0} \rightarrow S_{2,1} \rightarrow S_{3,2}, S_{3,4}$.
- Branch 3: $S_{0,0} \rightarrow S_{1,0} \rightarrow S_{2,0} \rightarrow S_{3,1}$.
- Branch 4: $S_{0,0} \rightarrow S_{1,0} \rightarrow S_{2,0} \rightarrow S_{3,0}$.

Figure 2 illustrates these branches in terms of angular separation and phase times. Figure 3 shows the phasing control for the final stage of each branch. Solving the phasing times in Branch 1 involves the most complexity, as the initial conditions of each stage are heavily dependent on the final conditions of the previous stage. In Branch 2, this complexity decreases because the solution becomes insensitive to the final conditions of Stage 1 (i.e., $k = 1$). This occurs because regardless of the time spent phasing $S_{1,1}$, $t_{k=1}$, the initial separation angle of the satellites in Stage 2 will always be zero, with its rate of change determined by the disengagement Δv and the orbital velocity at disengagement.

In Branch 3, this insensitivity extends to include the final conditions of Stage 3. Lastly, Branch 4 requires no consideration, as the initial and final conditions are always $\begin{bmatrix}\theta & \dot{\theta}\end{bmatrix} = [0\ 0]$ by definition. In other words, the optimal solution for $S_{3,\ 4\text{–}7}$ determines the value of $\theta_{1,1}$, and the optimal solution for $S_{3,\ 2\text{–}7}$ determines their respective $\theta_{2,i}$.

As the number of satellites increases, the disengagement sequence becomes increasingly complex. While the fundamental mathematical formulation remains consistent, the computational complexity grows due to the increased number of interactions and constraints that must be resolved. Specifically, the number of cases to analyze follows a logarithmic relationship, increasing with $(1 + \log_2 n)$.

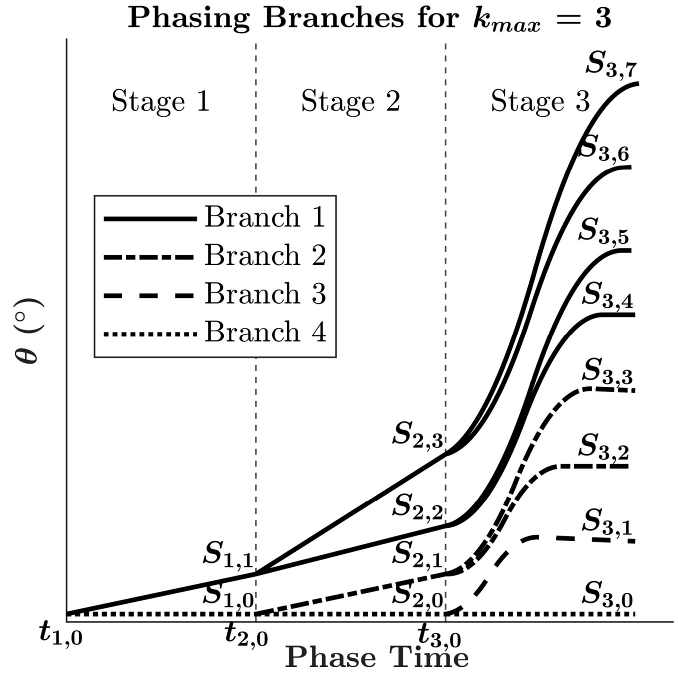

Figure 2. Plot showing phasing branches.

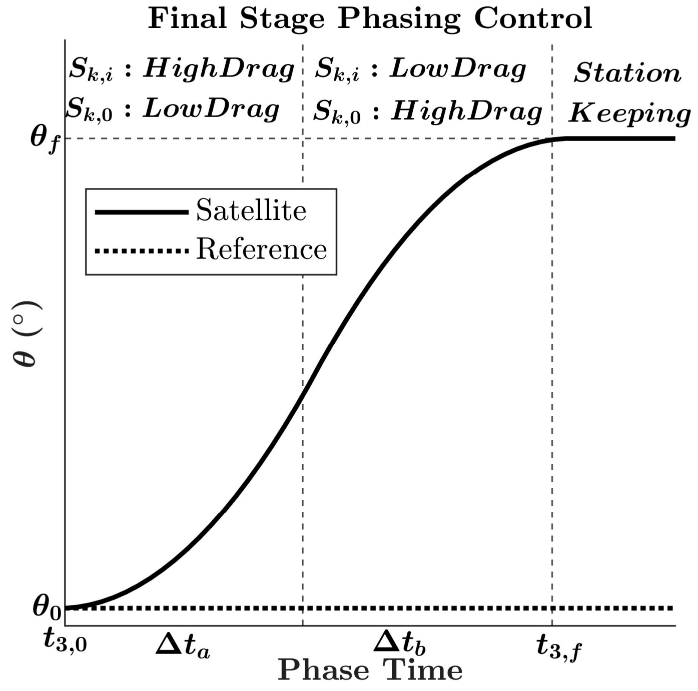

Figure 3. Phasing of the final-stage satellite.

2.5. The Deployment Problem

The goal of the deployment strategy is to minimize the total phasing time, $t_{phasing}$, which depends on the time spent in each deployment stage. Since, as shown in Equations (3) and (4), phasing times are governed by the initial and final relative motion, the objective is to determine suitable disengagement conditions at each stage that lead to an overall minimal phasing time, given by:

$$t_{phasing} = \sum_{k=1}^{k_{max}} t_k$$

where t_k denotes the phasing time at stage k.

Rather than solving this as a formal optimization problem, an enumerative simulation approach is adopted. This involves selecting and assessing a discretized set of candidate values for the imparted Δv and the angles of separation at which disengagement into the next stage occurs and calculating the resulting phase times. The combination of parameters that yields the shortest total phasing time is then selected as the most effective deployment strategy.

Since the final angular configuration of the constellation is a known mission parameter, the problem is formulated using a bottom–up approach. The final conditions at stage k_{max} are specified as $[\theta_{k_{max},\, i}\ 0]_f^T$, where $\theta_{k_{max},\, i_f}$ is the desired final separation angle of the i^{th} satellite within the range $[0,\ 360)$. The initial conditions of Stage k_{max} are determined by the angle at which disengagement occurs in the previous stage, $k = k_{max} - 1$, and the change in the relative motion due to the disengagement Δv. Whereby,

$$\theta_{k_{max},\, i_0} = \theta_{(k_{max}-1),\, i_f}\ and\ \dot{\theta}_{k_{max},\, i_0} = \dot{\theta}_{(k_{max}-1),\ i_f} + \Delta\dot{\theta}_{DM}$$

where $\Delta\dot{\theta}_{DM} = f(\Delta v_{DM})$. Consequently, $\left[\theta_{k_{max}-1,\, i}\ \dot{\theta}_{k_{max}-1,\, i}\right]_f^T$ represents the final relative motion of the penultimate stage. Once the initial conditions are found, Equations (3) and (4) can be employed to calculate Δt_a and Δt_b for the respective satellite.

Similarly for stages $k = 2,\ \ldots,\ k_{max}$, the initial conditions of a satellite depend on the final relative motion of its parent satellite in the previous stage and the disengagement Δv. For stage $k = 1$, the initial relative motion is determined solely by the disengagement Δv, as the initial separation angle will always be zero; therefore, $\theta_{1,1_0} = 0$ and $\dot{\theta}_{1,1_0} = \Delta\dot{\theta}_{DM}$.

The final solution is, therefore, a cascaded variant of the one provided by Foster et al. in [5], with the addition of the Δv imposed by the disengagement mechanism. Considering the case of an eight-satellite constellation requiring three deployment stages $(k = 3)$, the phasing problem would require solving for the variables collated in Table 2.

Table 2. Phasing problem variables ($k = 3$).

Variable	Initial Value	Final Value	Comments
$\theta_{1,\, 1}$	0	TBD	Final value is a decision variable
$\dot{\theta}_{1,1}$	$\Delta\dot{\theta}_{DMk=1}$	Depends on θ_{1,i_f}	Final value is coupled with $\theta_{1,\, i}$
$\theta_{2,\, i}$	θ_{1,i_f}	TBD	Final value is a decision variable
$\dot{\theta}_{2,i}$	$\dot{\theta}_{1,i_f} + \Delta\dot{\theta}_{DMk=2}$	Depends on θ_{2,i_f}	Final value is coupled with $\theta_{2,\, i}$
$\theta_{3,i}$	θ_{2,i_f}	[0, 360)	Final value depends on the satellite slot
$\dot{\theta}_{3,\, i}$	$\dot{\theta}_{2,i_f} + \Delta\dot{\theta}_{DMk=3}$	0	
$\ddot{\theta}_{1,i},\ \ddot{\theta}_{2,i},\ \ddot{\theta}_{3,i}$	-		Orbit dependent, calculated during simulation
$\Delta\dot{\theta}_{DM}$	$f(\Delta v_{DM})$		Calculated during simulation for different Δv

For each deployment stage, a reference–satellite pair will have unique values for $\left[\theta\ \dot{\theta}\right]_0^T$, $\left[\theta\ \dot{\theta}\right]_f^T$, and $\Delta\dot{\theta}_{DM}$. Therefore, for a given Δv and desired $[\theta_{k_{max},\, i}\ 0]_f^T$, the values of $\theta_{k,\, i_f}$ and $(\Delta t_a, \Delta t_b)_{k_{max}}$ that provide the optimal $t_{phasing}$ need to be found. Extending the solution to all n satellites in the constellation yields a set of $t_{phasing}$, the largest of which is the resulting total constellation phasing time.

Although the deployment strategy is evaluated using an enumerative simulation, the problem can still be expressed in terms of standard optimization components. Within this context, the objective function minimizes the total constellation phasing time such that:

$$min\ t_{phasing} = \max_{i}\left(\sum_{k=1}^{k_{max}} t_k\right)$$

where $t_{k,i}$ denotes the phasing time of satellite i at stage k, and the maximum ensures that the phasing is complete when the slowest satellite reaches its final relative position.

The decision variables include the disengagement velocity, $\Delta v_{DM,k,i}$, imparted to satellite i in stage k, and the final angular separation of the satellites, θ_{k,i_f}, in each stage k, for $k < k_{max}$. These variables are discretized and evaluated over a predefined search space in the simulation. Finally, the constraints of the deployment strategy include the following:

- The stage transition dynamics:

$$\theta_{k_{max},\ i_0} = \theta_{(k_{max}-1),\ i_f}$$

$$and\ \ \dot{\theta}_{k_{max},\ i_0} = \dot{\theta}_{(k_{max}-1),\ \ i_f} + \Delta\dot{\theta}_{DM};$$

- The final mission configuration: $\theta_{kmax,i_f} = \theta_i^{target}$, $\dot{\theta}_{kmax,i_f} = 0$;
- Angular separation bounds: $0 \ \leq\ \theta_{k,i_f} < 360$;
- Disengagement velocity limits: $\Delta v_{min}\ \leq \Delta v < \Delta v_{max}$.

2.6. Other Considerations

The initial relative motion is defined as $\left[\theta\ \dot{\theta}\right]_0^T$, where θ_0 is the initial separation angle, and $\dot{\theta}_0$ is its rate of change. These values typically depend on the deployment strategy imposed upon the launch vehicle, which defines the deployment direction, frequency, and velocity, as seen in the QB50 constellation [16]. However, unless multiple many-in-one systems are launched, this deployment sequence becomes less critical, as the proposed disengagement sequence inherently determines and controls initial relative motion.

However, orbital elements at deployment still impact differential drag phasing and phase times due to variations in atmospheric density. Mean atmospheric density is influenced by altitude, eccentricity, and solar activity. Lower altitudes and circular orbits experience higher densities, while atmospheric density at a given altitude increases with solar activity. Since dynamic pressure directly affects $\ddot{\theta}$ through differential drag, optimizing phasing times requires launching at lower altitudes, in circular or quasi-circular orbits, and during periods of high solar activity.

2.7. Problem Summary

In summary, the disengagement strategy for phasing the proposed deployment architecture requires careful consideration of several interdependent factors, including the initial orbit, the disengagement maneuver and its sequence, and the differential drag control method. The initial orbit serves as a mission design variable, constrained by launch availability and mission objectives. Given a specific initial orbit, the phasing sequence must be planned to achieve the final angular configuration of the constellation.

The desired final angular states define the constellation's operational layout. The deployment process involves determining the disengagement velocity Δv, the angular positions $\theta_{k,\ i_f}$ at intermediate stages, and the corresponding acceleration and deceleration durations $(\Delta t_a,\ \Delta t_b)_{k_{max}}$ for each satellite.

The phasing problem is inherently recursive, as the initial states and dynamics of the preceding stage shape the final conditions at each stage. Consequently, a bottom–up methodology is adopted, beginning with the known final configuration and propagating backwards through the deployment stages. This requires identifying appropriate insertion points at stage k_{Max} and determining the conditions under which each satellite should disengage and begin its phasing trajectory. Once the initial angular states and disengagement velocities are established for each stage, the total phasing time is obtained by summing the durations across all stages.

This formulation highlights the coupled nature of the deployment–dispersal dynamics, where each parameter influences the overall phasing performance. The following section outlines the simulation-based methodology used to assess this deployment problem.

3. Methodology

As discussed in Section 2, the parameters of interest, $\theta_{k,\, i_f}$ (from $k = 1\ to\ k_{max} - 1$) and $(\Delta t_a,\ \Delta t_b)_{k_{max}}$, increase in complexity with each deployment stage. However, this complexity can be mitigated through assumptions on satellite uniformity. Specifically, each disengagement stage reduces the satellite mass and surface area by half, while the drag coefficient remains constant. As a result, the maximum and minimum ballistic coefficients β_{Max} and β_{Min} remain unchanged across the early stages, ensuring that the angular acceleration $\ddot{\theta}$ remains constant during those phases.

Given this consistency, satellites with identical orbital parameters will phase at similar rates. However, due to the cumulative effects of disengagement Δv, satellites in later stages begin with greater relative separation rates. Therefore, initiating disengagements early is favorable, provided sufficient phasing time is allowed to prevent collisions. This assumption significantly simplifies the deployment analysis, reducing it to identifying the values of $\theta_{(k_{max}-1),\, i_f}$ and timing parameters $(\Delta t_a,\ \Delta t_b)_{k_{max}}$ that yield the shortest total phasing time.

The values of $(\Delta t_a, \Delta t_b)_{k_{max}}$ are determined analytically for each satellite–reference pair using Equations (3) and (4). Since the target constellation configuration predefines the final angular separations and the control authority $\ddot{\theta}$ is updated throughout the simulation, the unknowns reside in the initial conditions at stage k_{max}, which are derived from the preceding stage. This is achieved by generating a set of candidate insertion points for each satellite at the penultimate stage. To resolve this, the phasing problem is reformulated as identifying the set of insertion angles $\theta_{(k_{max}-1),\, i_f}$ that minimize the total phasing time.

Each satellite is phased towards discrete angular targets, $\theta \in \{0, \Delta\theta, 2\Delta\theta, \ldots, 360\}$, followed by the application of a disengagement Δv. This process is summarized in Algorithm 1, which outputs the resulting initial relative motions and the associated timing values $t_{(k_{max}-1),\, i}$.

Subsequently, Algorithm 2 computes the phasing durations $(\Delta t_a, \Delta t_b)$ for each candidate insertion point, which formed the output of Algorithm 1, using the analytical solution. The combination that yields the shortest sum of Δt_a, Δt_b, and $t_{(k_{max}-1),\, i}$ is identified as the most favorable. This simulation process is repeated for all $n - 1$ satellites in the final deployment stage.

The longest of these values defines the final phasing time for the constellation, as it represents the slowest-converging satellite relative to the reference. This value is then used to determine the final phasing segment for the last satellite–reference pair.

For instance, for a system of eight satellites and $k_{max} = 3$, the output will consist of optimal values for $t_{2,\, 1}$, $t_{2,\, 2}$, and $t_{2,\, 3}$, calculated for satellites $S_{2,1}$, $S_{2,2}$, and $S_{2,3}$, covering the branches from Section 2.4. The largest of these values defines the reference timing for the final stage.

Throughout this process, Δv is assumed constant across all disengagements and is scaled proportionally to satellite mass. To determine the most effective Δv magnitude, Algorithms 1 and 2 are executed over a predefined range of candidate values. The value yielding the shortest total phasing time among the tested configurations is selected. Top-level flow charts of Algorithms 1 and 2 are illustrated in Figures 4 and 5, respectively.

The algorithms are employed as follows: First, the initial orbital parameters, satellite properties, and epoch of the single-unit satellite are input into Algorithm 1, along with the disengagement velocity vector and its direction in the LVLH reference frame. The algorithm begins by propagating the satellite to its first perigee, where the initial disengagement is applied (Algorithm 1, Lines 1–3).

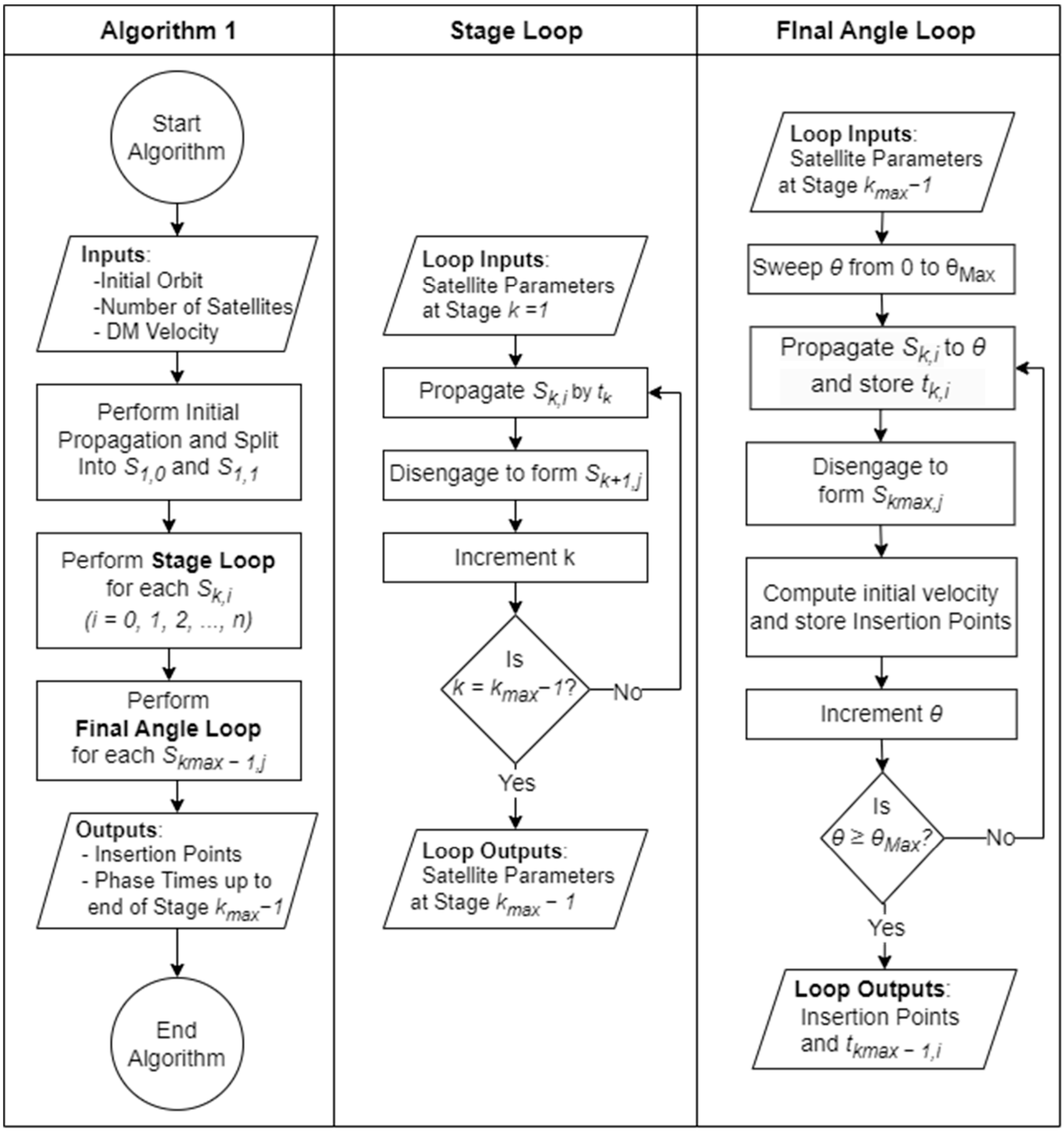

Figure 4. Algorithm 1 top-level flow chart.

Following this, the two resulting satellites are each propagated for a fixed interval, t_k, to allow for sufficient separation and prevent collisions prior to the next disengagement event. In this study, t_k is set to 7 days. After this interval has elapsed, both satellites are propagated to their respective next perigees, where the subsequent disengagement occurs.

This process is iteratively repeated until the penultimate stage is reached (Algorithm 1, Lines 4–7).

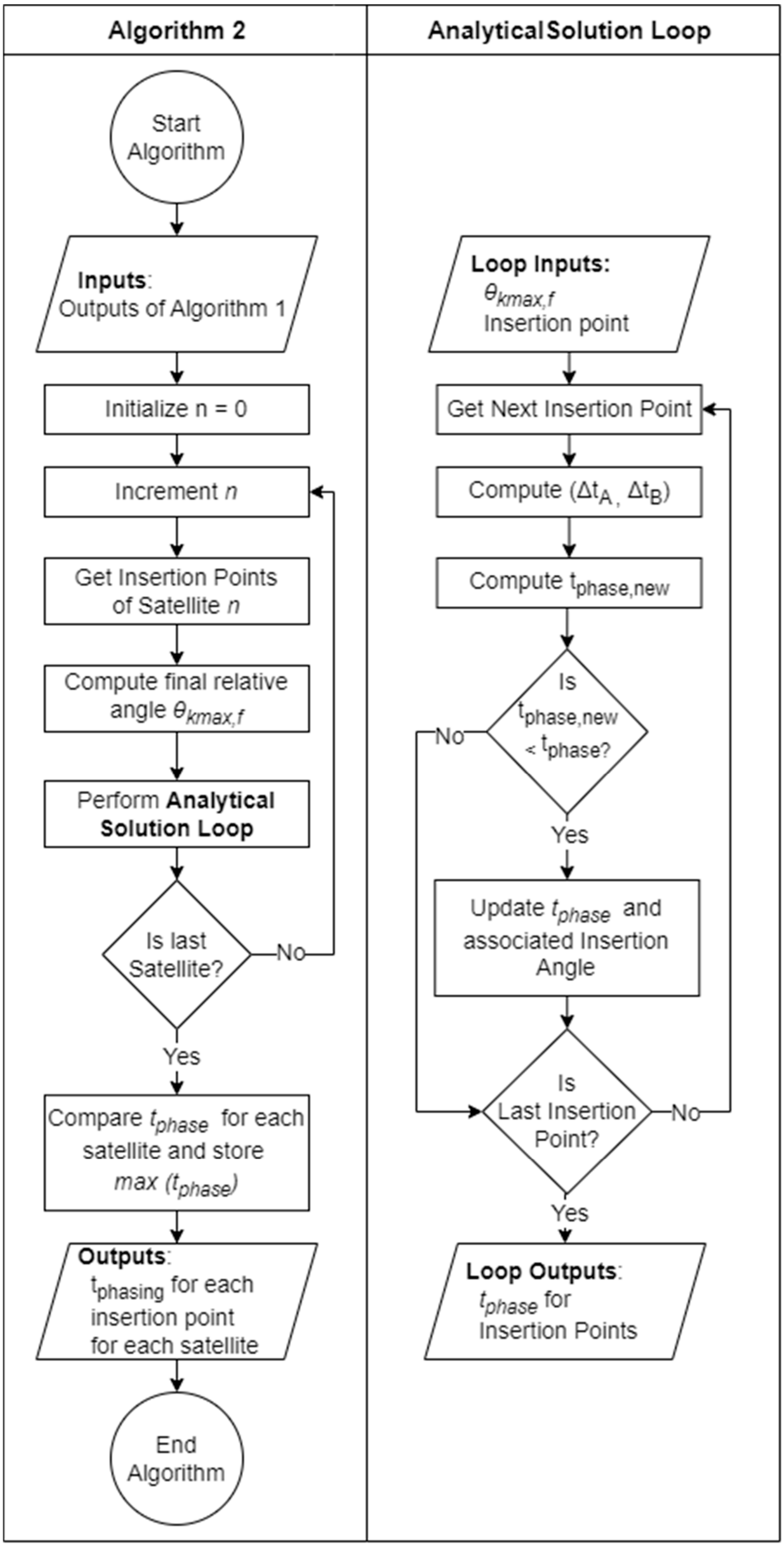

Figure 5. Algorithm 2 top-level flow chart.

Algorithm 1: Generate Stage k_{max} Insertion Points

```
1:  Procedure: Generate Stage $k_{max}$ Insertion Points
2:  Propagate $S_{0,0}$ until the first disengagement command.
3:  Perform $S_{0,0}$ disengagement maneuver to obtain $S_{1,1}$ and $S_{1,0}$
4:  for $k = 1; k < k_{max} - 1; k$ ++, do
5:          Propagate $S_{k,i}$ by $t_k$ and to next perigee
6:          Perform $S_{k,i}$ disengagement maneuvers to obtain $S_{k+1,j}$
7:  end for
8:  for $i = 1; i < 2^{k_{max}-1}; i$ ++, do
9:      for $\theta_{(k_{max}-1),\, i} = 0;\ \theta_{(k_{max}-1),\, i} < \theta_{(k_{max}-1),\, i\ max};\ \theta_{(k_{max}-1),\, i} + \Delta\theta$ , do
10:             Propagate $S_{(k_{max}-1),i}$ until $\theta_{(k_{max}-1),\, i}$ , store $t_{(k_{max}-1),\, i}$
11:             Perform $S_{(k_{max}-1),i}$ to $S_{(k_{max}),j}$ disengagement maneuver
12:             Calculate $S_{(k_{max}),j}$ initial relative motion (insertion points)
13:     end for
14: end for
15: Output: $S_{k_{max},\, j}$ insertion points for every $\theta_{(k_{max}-1),\, i}$ and associated $t_{(k_{max}-1),\, i}$
```

Algorithm 2: Calculate Optimal Phasing Times

```
1:  Procedure: Final Stage Optimal Phase Time
2:  for $i = 1; i < n; i$ ++, do
3:      Get $S_{k_{max},\ i}$ insertion points from Algorithm 1 output
4:      Get $S_{k_{max},\ i}$ final angular separation through $\theta_{k_{max},\, i_f} = 360\left(1 - \frac{1}{n}\right)$
5:      for number of insertion points, do
6:          Calculate $(\Delta t_a, \Delta t_b)_{k_{max},i}$ through Equations (3) and (4)
7:          Equate $t_{phase,new} = (\Delta t_a, \Delta t_b)_{k_{max},i} + \sum_{k=1}^{k_{max}-1} t_k$
8:          if $t_{phase,new} < t_{phase}$
9:              $t_{phase} \leftarrow t_{phase,new}$
10              $\theta_{(k_{max}-1),\ j_f} \leftarrow \theta_{k_{max},i_0}$
11:         end if
12:     end for
13: end for
14: Compare all $t_{(k_{max}-1),j_f}$ , largest value = $t_{(k_{max}-1)}$
15: Output: $t_{(k_{max}-1)}$ and $(\Delta t_a, \Delta t_b)_{k_{max},i}$ for $i = 1,\ 2,\ \ldots,\ (n-1)$ .
```

At the penultimate stage, each satellite is propagated until it reaches a discretized set of angular separations relative to a designated reference satellite. Upon reaching the target angular separation, the satellite is propagated to its subsequent perigee, where the final disengagement takes place. The resulting relative angular velocity and separation angle at this point are recorded, forming an insertion point $\left[\theta\ \dot{\theta}\right]_i^{k_{max}}$. This process is repeated for all satellites in the penultimate stage until an insertion point has been obtained for every value in the discretized angle set (Algorithm 1, Lines 8–14).

Once the complete set of insertion points has been generated, it is passed to Algorithm 2, along with the desired final angular separation for the last-stage satellites. In Algorithm 2, each insertion point is evaluated using the target separation and Equations (3) and (4), which determine the required phasing times (Algorithm 2, Lines 3–6). The total phase time for a given final-stage satellite is computed by summing the phasing contributions from each stage with the time derived from Equations (3) and (4).

Each total phase time is compared against those obtained from other insertion points, and the smallest value is retained as the best-case phase time for that satellite. This process is repeated for all insertion points associated with each final-stage satellite and then again across all final-stage satellites (Algorithm 2, Lines 2–13). The maximum among these best-case satellite values is taken as the best-case phase time for the whole constellation.

In practice and in the following case studies, the phase time of each satellite at every insertion point is stored and plotted, enabling enumerative analysis of phasing performance across the complete set of candidate configurations.

In summary, the deployment analysis focuses on minimizing the total phasing time $\sum_{k=1}^{k_{max}} t_k$. Since the ballistic coefficients are constant up to $k = (k_{max} - 1)$, the corresponding phase durations are minimized while ensuring adequate separation. The problem is therefore reduced to evaluating candidate values for $\theta_{(k_{max}-1),\, i_f}$ and the final-stage timing parameters $(\Delta t_a,\ \Delta t_b)_{k_{max}}$ across a range of Δv. This parameter sweep defines the performance envelope of the disengagement mechanism and enables identification of the configuration yielding the shortest total phasing time.

4. Case Studies

To demonstrate the feasibility of the proposed dispersal method and the impact of disengagement velocity and phase angle selection on phasing times, two case studies are presented. The first case study presents a system of eight PocketQube-sized satellites in an initial configuration resembling a 1U CubeSat. The second presents the case of four 1U CubeSat satellites in a 2 × 2 × 1 initial configuration.

The simulations are performed using the MATLAB R2024a Aerospace Blockset. In both case studies, the initial perigee altitude is set to 500 km, matching standard rideshare options, with an eccentricity of 0.01. Other orbital elements are set to zero and are summarized in Table 3.

Table 3. Simulation initial orbit setup.

Orbital Element	Initial Value
Epoch	1 December 2020
Altitude (perigee)	500 km
Eccentricity	0.01
Inclination	Case Study 1: 90° Case Study 2: 63.4°
RAAN	0°
Arg. of perigee	0°
True anomaly	0°

The motion models used for the case studies are governed by the high-precision numeric orbital propagator in MATLAB's Aerospace Toolbox. The initial orbital position and velocity are presented in the ICRF inertial frame. The block computes the acceleration acting on the satellite from the perturbation models such that:

$$\vec{a}_{ICRF} = \vec{a}_{CentralBody} + \vec{a}_{ThirdBody} + \vec{a}_{Drag} + \vec{a}_{SRP}$$

where $\vec{a}_{CentralBody}$ is the acceleration due to the gravitational potential of Earth using the EGM2008 spherical harmonics model, $\vec{a}_{ThirdBody}$ is the acceleration due to the Moon and the Sun modeled as point masses, and $\vec{a}_{SRP}$ is the acceleration caused by Solar Radiation

Pressure (SRP) and equated in conjunction with a dual-cone shadow model for eclipse. Additionally, $\vec{a}_{Drag}$ is the acceleration due to atmospheric drag obtained from the equation:

$$\vec{a}_{Drag} = \frac{1}{2}\rho\left(\frac{c_D A}{m}\right)v_{rel}^2\frac{\vec{v}_{rel}}{v_{rel}}$$

where v_{rel} is the satellite velocity relative to the atmosphere. The atmospheric density is obtained from the NRLMSISE-00 atmospheric model in conjunction with CelesTrak space weather data. The epoch is set during the solar minima of Solar Cycle 25, leading to reduced atmospheric densities and lower differential accelerations, which present the worst-case weather conditions for a dispersal method dependent on drag. The EGM2008 and NRLMSISE-00 models were selected due to them being readily available in MATLAB. Additionally, NRLMSISE-00 has become the standard for satellite drag modeling over the last few years [17].

These accelerations are summed and integrated using MATLAB's ode113 solver, as it is well suited for smooth, non-stiff orbital dynamics to propagate satellite state in the ICRF frame. The disengagement-induced change in velocity was modeled as an instantaneous impulse in the LVLH frame, transformed into the ICRF frame, and manually applied to the velocity vector at the moment of separation.

4.1. Case Study 1: The PQ8 Satellite

The first case study examines the PQ8, a constellation under development at the University of Malta and illustrated in Figure 6. The PQ8 is a 1U CubeSat (10 × 10 × 10 cm^3 with a mass of 2 kg) hierarchically assembled from eight PQ1 satellites. Each PQ1 is formed by slicing the PQ8 in half twice, lengthwise and heightwise, resulting in eight 5 × 5 × 5 cm units, each weighing 250 g, closely resembling a 1p PocketQube in size and shape.

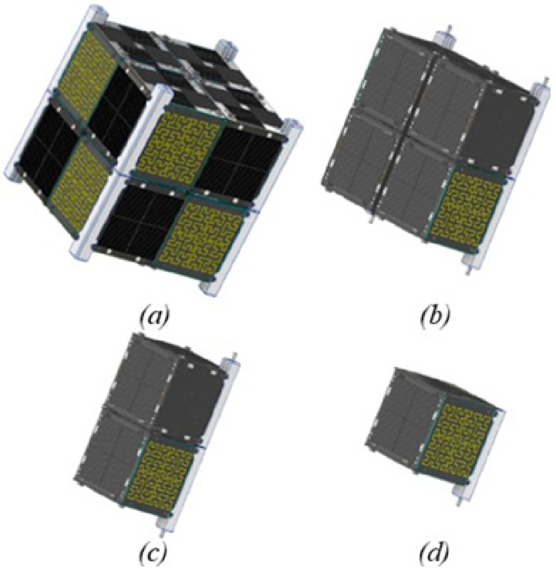

Figure 6. (**a**) PQ8 satellite. (**b**) PQ4 satellite. (**c**) PQ2 satellite. (**d**) PQ1 satellite.

The deployment sequence follows the architecture proposed in this article, forming intermediate configurations—PQ8 → PQ4 → PQ2 → PQ1—as depicted in Figure 6a–d. The process begins with the PQ8 ($S_{0,0,}$) at $k = 0$, which undergoes an initial disengagement maneuver, splitting into two PQ4 satellites ($S_{1,i}$) at $k = 1$. These are phased before further splitting into PQ2 satellites ($S_{2,i}$) at $k = 2$, and finally, eight independent PQ1 satellites ($S_{3,i}$) at $k = 3$.

To model aerodynamic effects, the drag coefficients were first obtained, using the method proposed by Moe et al. in [18] and outlined in Appendix A. The ballistic coefficients were then obtained through $\beta = m/sc_D$. Table 4 presents the results, showing the ballistic coefficients for the PQ4, PQ2, and PQ1 stages. The PQ4 and PQ2 stages have identical ballistic coefficients, as their mass and surface area scale proportionally. In contrast, transitioning from PQ2 to PQ1 involves halving the mass while maintaining the same surface areas. To achieve this increased area and enhance differential drag in the PQ1 configuration, a deployable panel was added to the design.

Table 4. PQ8 ballistic coefficients.

Satellite	**Maximum**		**Minimum**	
	Ram Surface	**β (kg/m^2)**	**Ram Surface**	**β (kg/m^2)**
PQ4	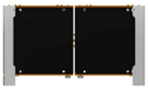	57.2	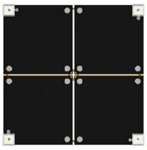	28.6
PQ2	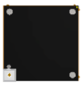	57.2	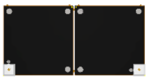	28.6
PQ1	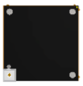	28.6	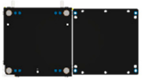	14.3

4.1.1. Initial Relative Motion

The initial relative motion between satellites was determined by computing the angle between their position vectors. Depending on the drag configuration, this angle either increases or decreases over time. It also exhibits oscillatory behavior due to orbital variations between apogee and perigee. Figure 7 illustrates this behavior across multiple orbital cycles. The first and second derivatives of the angular separation yield the relative angular velocity and angular acceleration. To accurately capture the average angular acceleration, values are extracted from extended simulation periods. As shown in Figure 7d, the average converges to a stable value of $0.0103°/\mathrm{day}^2$ after approximately 140 days, despite initial variability.

4.1.2. Disengagement Velocity and PQ1 Insertion Points

The initial angular velocity of each satellite increased linearly with respect to an increase in disengagement velocity, as illustrated in Figure 8. The PQ1s that have experienced multiple positive Δv instances exhibit higher initial separation rates. For example, $\mathrm{PQ1}_7$, having undergone three successive positive, exhibits the highest initial angular velocity. $\mathrm{PQ1}_6$, $\mathrm{PQ1}_5$, and $\mathrm{PQ1}_3$ follow accordingly, while the remainder experienced lower separation rates due to fewer positive Δv increments.

The insertion points represent the $\left[\theta\ \dot{\theta}\right]_0^T$ values for each PQ1 satellite in the PQ1 phase. These values depend on both the disengagement velocity and the relative positions of the satellites at the time of disengagement, as illustrated in Figure 9. The separation rates are grouped similarly to those described by the disengagement velocity in Figure 6. Notably, oscillations in the plots highlight the influence of the epoch at disengagement on the resulting relative angular velocities.

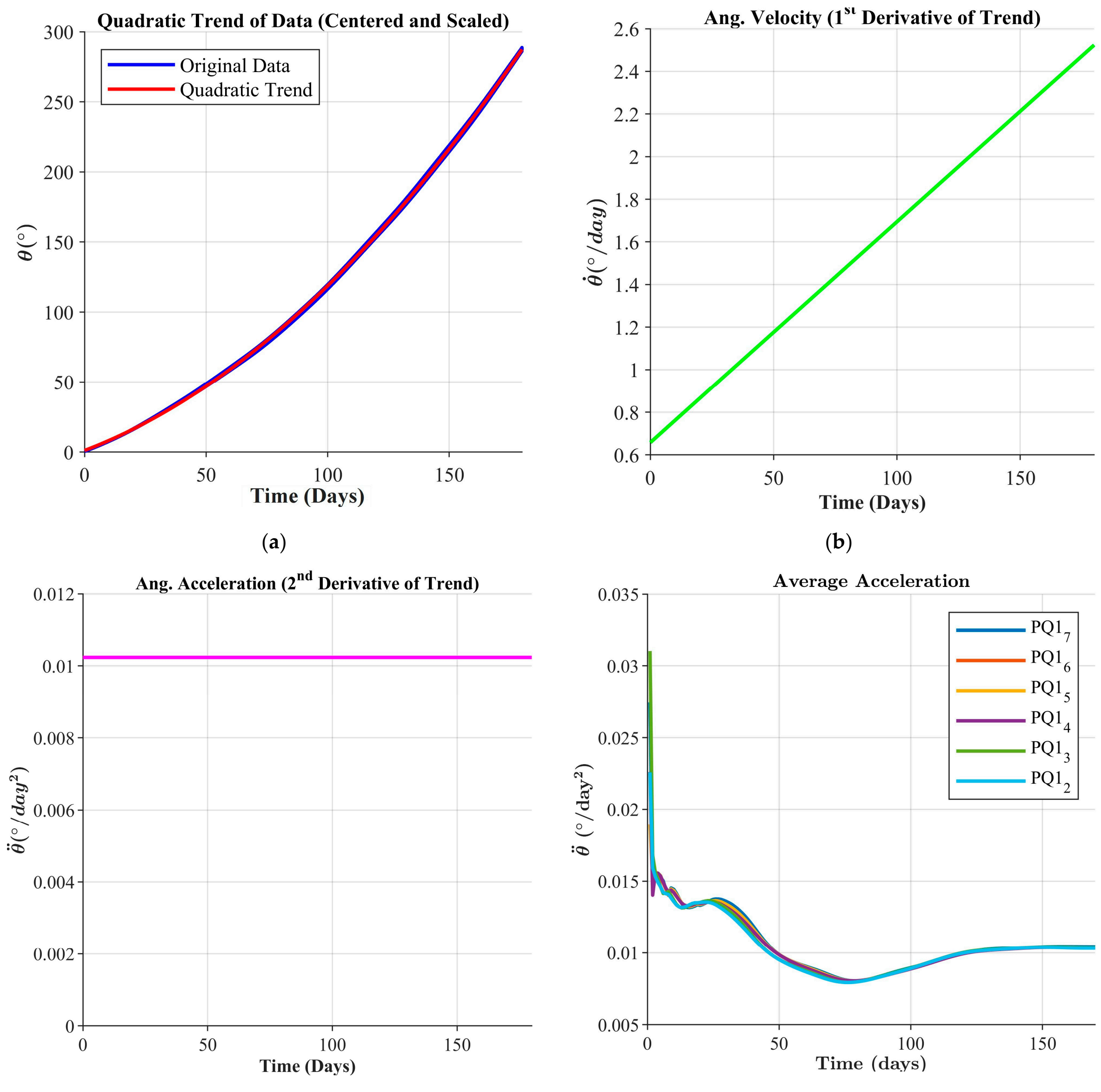

(**a**) (**b**)

(**c**) (**d**)

Figure 7. (**a**) PQ satellite relative motion: relative angle, (**b**) angular velocity, (**c**) angular acceleration, and (**d**) average acceleration.

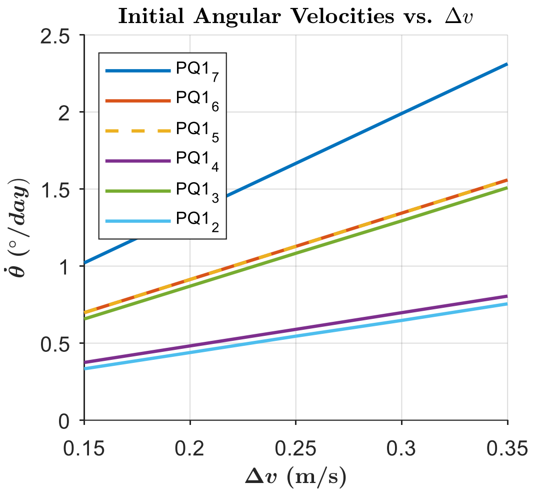

Figure 8. PQ1 initial angular velocities.

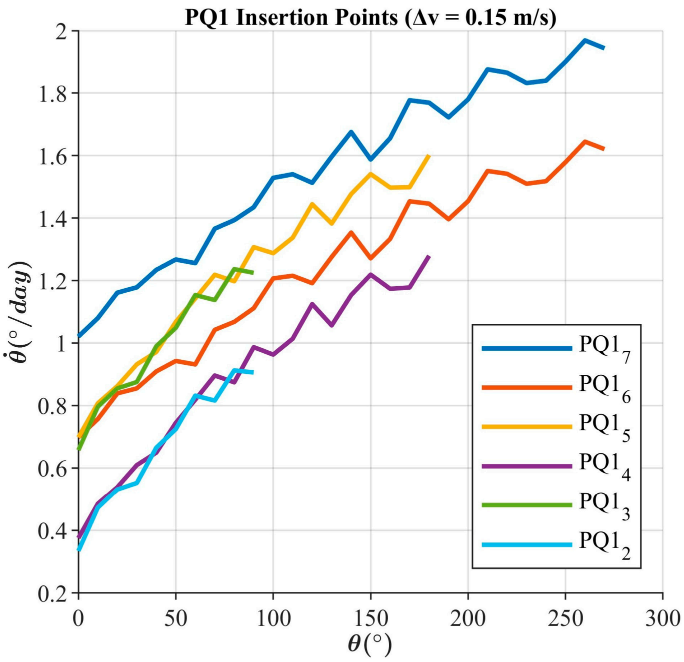

Figure 9. PQ1 insertion point for $\Delta v = 0.15\ \mathrm{ms}^{-1}$.

4.1.3. Constellation Phase Times

Figure 10 depicts the phase times for $PQ1_7$ for various Δv magnitudes with respect to $\theta_{PQ1,initial}$. The plot for the largest Δv magnitude, 0.35 m s^{-1}, shows the quickest phasing times. Notably, all cases start with a gradual gradient before rapidly increasing to match the gradients of the other plots. The gradual gradient occurs when the reference satellite is the first to enter the low-drag configuration post-disengagement, while the other PQ1 remains in high-drag mode. During this period, the phasing time is not sensitive to changes in $\theta_{PQ1,initial}$, as reflected by the slight gradient. However, after a certain threshold value, $\theta_{PQ1,thresh}$, the gradient increases sharply. Beyond this point, the reference satellite is in high-drag mode immediately following disengagement, with the other PQ1 in low drag, making phasing times highly sensitive to $\theta_{PQ1,initial}$.

Additionally, disengagement performed at $\theta_{PQ1,thresh}$ introduces an edge condition in which the acceleration phase is entirely omitted, as the peak separation velocities are reached through the disengagement Δv's alone and, thus, require only deceleration to achieve the desired relative angular separation.

As $\dot{\theta}_i$ is linearly proportional to the disengagement Δv, an increase in Δv reduces $\theta_{PQ1,thresh}$. At Δv magnitudes of about 0.4 m s^{-1} or greater, the slight gradient would no longer be present. This suggests that increasing the Δv magnitude beyond a certain threshold, Δv_{thresh} is not viable. In this case, Δv_{thresh} would be about 0.4 m s^{-1}.

Comparing the plots indicates that increasing the Δv magnitude while remaining below Δv_{thresh} results in better phasing times in the small-gradient region. This implies that the optimal phase times occur when $\Delta v = \Delta v_{thresh}$ and that there is a trade-off between Δv, phase times, and the range of viable $\theta_{PQ1,initial}$.

If the best-case Δv magnitude is used, any delay in the PQ2-to-PQ1 disengagement will cause a significant increase in phase times as the solution shifts into the large-gradient region. Conversely, when Δv is less than Δv_{thresh}, a window exists in which delays have little impact on phase times. This window could be leveraged to accommodate necessary delays for disengagement maneuvers, such as collision avoidance or fault handling.

Among the Δv magnitudes simulated for this scenario, the 0.35 m s^{-1} value provided the best phasing time, approximately 255 days. However, this represents the phasing time for $PQ1_7$, with the other satellites reaching their phase angles more quickly, as shown in Figure 11. In each simulation, the total phase time was determined by the phasing time of $PQ1_7$. This insight could be used to reduce simulation times in future analyses by focusing primarily on the phasing of the leading satellite, $S_{kmax,n-1}$.

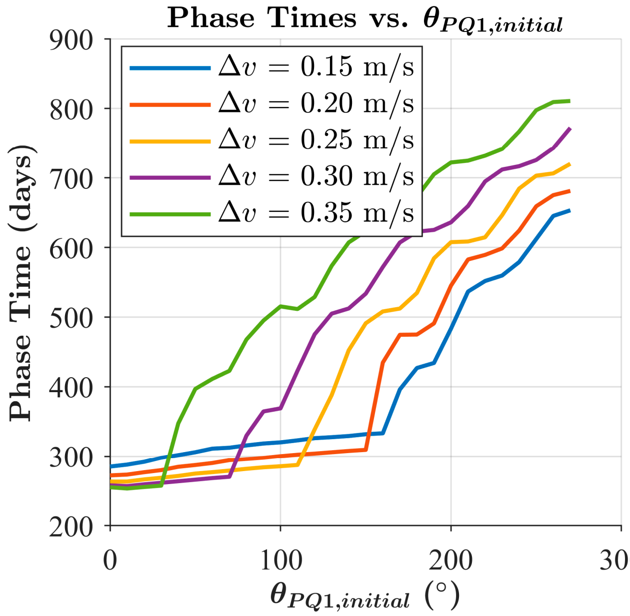

Figure 10. Phase times for $PQ1_7$ for various Δv magnitudes.

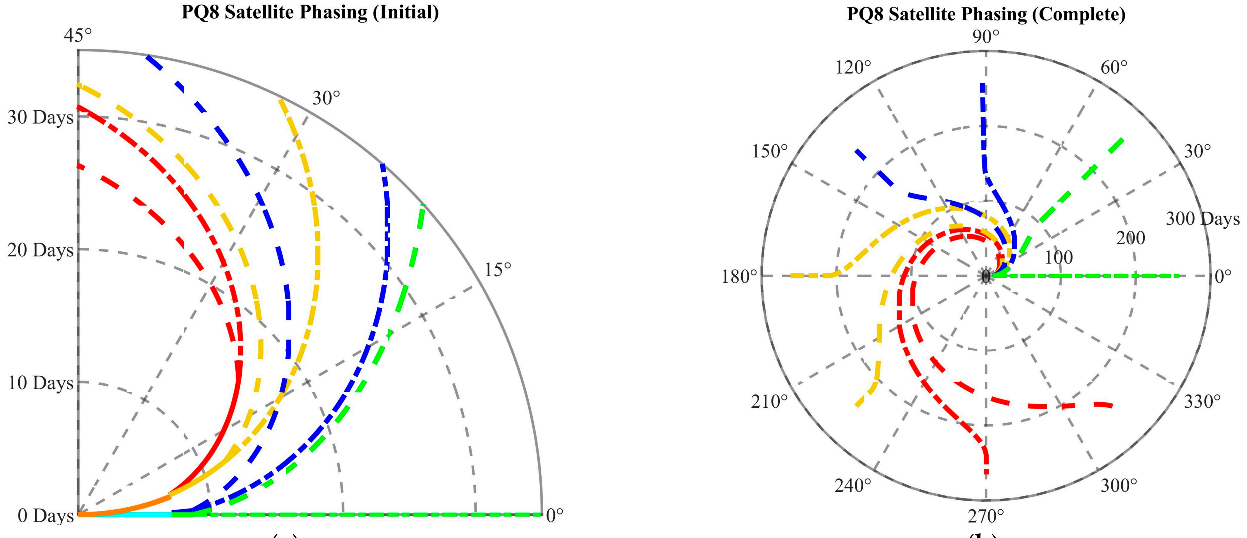

(**a**) (**b**)

Figure 11. (**a**) Early orbit separation (note the scaled theta axis). (**b**) PQ8 satellite phasing polar plots.

To achieve this phase time, perfect attitude control is assumed. In practice, Alba Orbital has demonstrated that their Unicorn-2 PocketQube can attain a pointing accuracy of approximately 5° ("Unicorn-2 Features and Specifications," Alba Orbital, Glasgow, Scotland, 2019. https://www.albaorbital.com/unicorn-2-features-and-specifications (accessed 14 April 2025)). Considering a worst-case scenario where both the satellite and the reference exhibit this level of inaccuracy, the resulting range of ballistic coefficients spans from 14.5 to 29 kg m^{-2} for the final phase. This variation yields an average angular acceleration of 0.0102° day^{-2} and a corresponding phase time of approximately 256.5 days.

The output Δv values indicate the change in velocity required in the in-track direction for the desired orbital phase times to be achieved. In practice, the pointing accuracy of the mechanism also needs to be considered. Considering the case of a 0.35 m s^{-1} disengagement and the same pointing accuracy of 5°, this would result in in-track and cross-track velocity components of 0.3486 m s^{-1} and 0.0306 m s^{-1}, respectively. Simulating these conditions with this 5° uncertainty yields a maximum phase time of approximately 256.53 days, an increase of approximately 45 min. The small increase in phase time is attributed to the slight decrease in initial angular velocities. Similarly, the cross-track component is too small to produce any meaningful change in the orbital dynamics.

As presented in Appendix A, the case studies were performed under the assumption that 90% of the incident atmospheric particles re-emitted from the satellite surface were diffuse, with the remainder being quasi-specular. To assess the sensitivity of this assumption, the simulations were extended to explore cases with f values of 0.85 and 1, where a value of 1 corresponds to a completely diffuse reflection. The ballistic coefficient of the PQ1 satellite at these f values becomes 28.2 and 28.8, respectively, accounting for a 5° uncertainty introduced by the attitude control subsystem. For a relative velocity of 0.35 m s^{-1}, these ballistic coefficients result in phase times of 254 and 256.8 days, respectively.

Table 5 collates the phase times discussed in this section, including those of the ideal case, the attitude control uncertainty on differential drag, the attitude control uncertainty on the disengagement direction, and the uncertainty on the estimation of the ballistic coefficient. The pointing and modeling tolerances introduce an uncertainty of approximately $+2/-1$ days over the ideal case phase time. While this uncertainty is relatively minor, larger discrepancies in the phase time are expected due to the more significant uncertainties inherent in the atmospheric model. Variations in the atmospheric density, composition, and temperature are not adequately captured and introduce inaccuracies that remain the dominant sources of error in differential drag control simulations.

Table 5. Phase times uncertainties ($\Delta v = 0.35$ ms^{-1}).

Case	Conditions	Phase Time
Ideal	No ADCS inaccuracy, f = 0.9	255.0 days
ADCS inaccuracy	±5° during dispersal only, f = 0.9	256.5 days
	±5° during dispersal and disengagement, f = 0.90	256.5 days
ADCS inaccuracy + BC Modeling	±5° during dispersal and disengagement, f = 0.85	254.0 days
	±5° during dispersal and disengagement, f = 1.00	256.8 days

4.1.4. Semi-Major Axis Decay and RAAN Drift

Since the system relies on differential drag control, it inherently induces a difference in the semi-major axis between the satellites. This presents two key concerns. First, a difference in the semi-major axis leads to a variation in the satellites' mean motion, causing the in-plane phase angle to drift apart. Second, it causes differential nodal precession within the constellation.

The first concern is mitigated by the differential drag control strategy, particularly through the analytical solutions provided in Equations (3) and (4). These equations are solved to ensure a final angular separation rate $\dot{\theta}$ of zero, which directly correlates with mean motion. Essentially, the differential drag controller reduces the semi-major axis of the higher-altitude satellite at a faster rate than that of the lower-altitude satellites until they converge to approximately the same value. As a result, their mean motions become nearly identical. This effect is illustrated in Figure 12, which shows the semi-major axis profiles of the leading PQ1 satellite and the reference satellite. Here, the reference satellite, $PQ1_0$, is in high-drag mode, until its mean motion converges with that of $PQ1_7$, which is in low-drag mode.

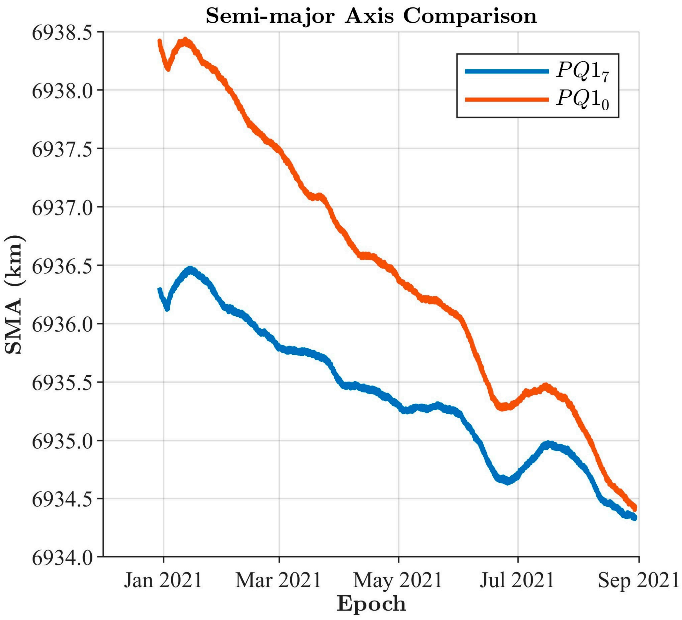

Figure 12. Semi-major axis comparison between the leading satellite and the reference.

The second concern remains valid, as some drift in RAAN between satellites is inevitable when using this method for dispersal. The formula for nodal precession is given by:

$$\dot{\Omega} = -\frac{3}{2}\left(\frac{R_E}{(a(1-e^2))}\right)^2 J_2 \omega \cos(i)$$

where R_E is Earth's radius, a is the semi-major axis, J_2 is Earth's second dynamic form factor, ω is the angular velocity of the satellite, e is the eccentricity, and i is the inclination. The extent of this drift is strongly influenced by orbital inclination. At high inclinations, particularly near-polar orbits, RAAN drift is minimal, due to the term $\cos(i)$, and negligible over typical phasing durations. However, at lower inclinations, the effect can become more pronounced, with drift reaching several degrees depending on the length of the deployment phase. In general, a shorter phasing period helps minimize this divergence. The degree of RAAN drift that can be tolerated is ultimately mission dependent. In this context, Falcone et al. proposed a differential drag control scheme that addresses cross-track motion using convex optimization [12]. If nodal precession poses a concern for constellation geometry or coverage, such schemes can be integrated to help mitigate its long-term impact.

4.2. Case Study 2: A 4U CubeSat

In the second case study, a fictitious scenario is considered in which the constellation consists of four 1U CubeSats, collectively referred to as CS4. These satellites are initially stacked in a configuration similar to the PQ4 satellite shown in Figure 6b. Each unit, denoted as CS1, has a mass of 2 kg and a deployable panel with an area of 0.01 m^2. Using the same configurations presented in Table 4 but scaled for mass and area yields β_{Max} and β_{Min} values of 114.4 and 57.2 kg m^{-2}, respectively, for the CS2 satellites. In the case of the CS1 satellites, the corresponding values are 57.2 and 28.6 kg m^{-2}, respectively.

The deployment strategy begins at the CS4 stage, where the satellite maintains its 4U CubeSat form factor. Its deployment follows a k_{max} = 2 stage deployment process, starting with the initial launch of a CS4 satellite at $k = 0$. After an initial disengagement maneuver, the CS4 satellite splits into two CS2 satellites, marking the start of stage $k = 1$ and phased to some degree. The process is then repeated, culminating in four CS1s.

4.2.1. Constellation Phase Times

Figure 13 illustrates the phase times for $CS1_3$ across various Δv magnitudes. The trends closely follow those observed in the PQ8 case study, remaining within a similar range of phase times. This consistency suggests that the proposed algorithms scale reliably across different constellation sizes and configurations. In this case, a Δv magnitude of 0.45 $\mathrm{m\,s^{-1}}$ provided the best phase times of approximately 331 days.

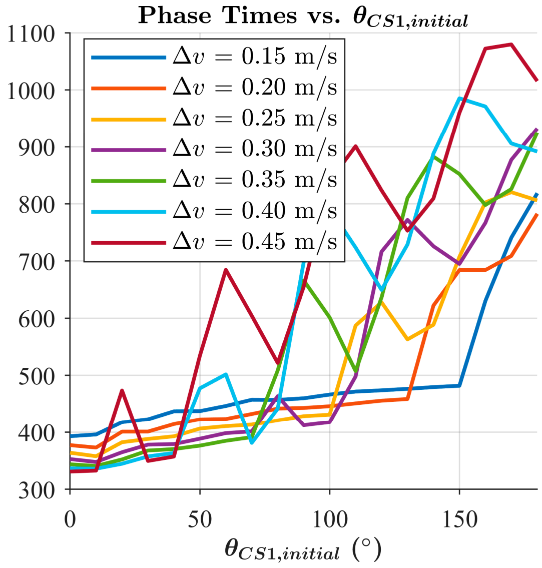

Figure 13. Phase times for $CS1_3$.

The required Δv magnitude for the disengagement mechanism increased despite the proportional scaling of mass, with Δv_{thresh} almost double that of Case Study 1. This increase is attributed to the reduction in the number of disengagement sequences, from the three-stage process in the PQ8 case to the two-stage process in the CS4 study. This trend suggests that as the number of satellites in the constellation increases, the demand on the disengagement mechanism decreases. This outcome is intuitive, as a larger number of satellites results in more Δv instances, distributing the required impulse more effectively. However, when considering Δv_{thresh} alongside the collision avoidance trade-off discussed in the previous case study, it becomes evident that an upper limit exists on the number of satellites in the constellation. Beyond this, Δv_{thresh} falls below the minimum required to prevent collision.

4.2.2. Ballistic Coefficient and Phase Times

In both case studies, a single deployable surface was assumed to achieve a ballistic coefficient ratio of 2:1. Increasing the ballistic coefficient, whether through additional deployables or alternative methods, can substantially reduce phase times. For instance, if all four sides of the cube-shaped satellites were deployable, a ballistic coefficient ratio of 5:1 would be achieved, leading to significantly improved phase times, as illustrated in Figure 14. Moreover, this benefit could be further improved, as the analysis does not consider the potential increase in disengagement Δv. A higher ballistic coefficient ratio raises the Δv_{thresh} value, thereby enabling a greater separation velocity.

Furthermore, although both case studies employed a ballistic coefficient ratio of 2:1, the rate of separation differed due to the absolute values of the ballistic coefficients. The case with the lower β values achieved faster phase times than the one with higher β values. This is because differential drag acceleration is not governed by the ratio alone but more so by the difference in inverse ballistic coefficients, as shown in Equation (2). Lower absolute ballistic coefficients yield stronger drag forces and, thus, faster acceleration rates.

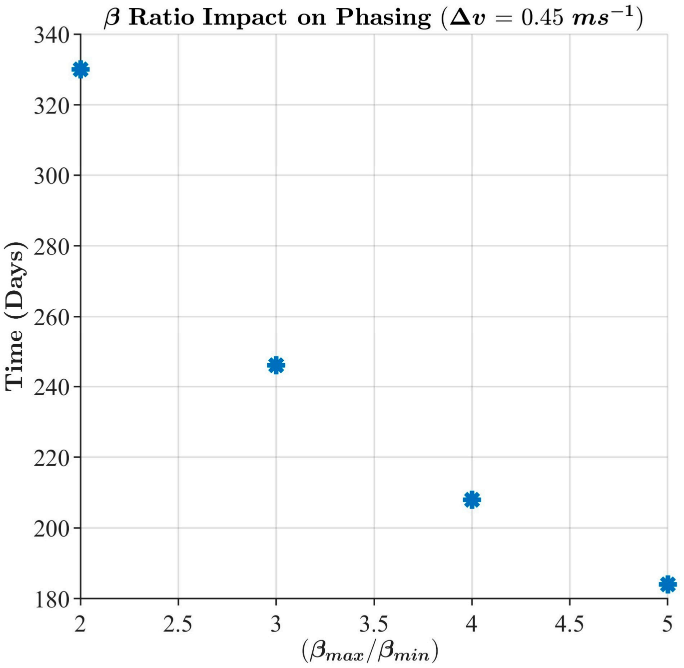

Figure 14. Ballistic coefficient ratio effect on phase times.

When combined, the effects of differential drag scaling with absolute ballistic coefficients and the cumulative impact of the disengagement Δv lead to significantly reduced phasing times. This suggests that the proposed method is particularly well suited to constellations composed of a larger number of compact, mass-optimized satellites.

4.3. Summary of Results

The case studies presented demonstrate the feasibility and performance of the proposed dispersal method for deploying a single-plane constellation from a single launch. The results highlight the significance of selecting the disengagement velocity Δv and the insertion angle $\theta_{initial}$, both of which directly influence phasing times.

Simulations confirm that by adjusting Δv to within a given range, the phasing time can be significantly reduced. Additionally, the identification of a disengagement window, governed by the critical angle θ_{thesh}, provides flexibility, as planning for disengagement before this threshold is reached allows the system to tolerate operational delays without major performance degradation.

In the case of the PQ8 architecture, the total phasing time was approximately 255 ± 1.5 days. This indicates that the proposed method is not only feasible but also particularly viable for missions involving small, mass-constrained satellite platforms. Collectively, the results demonstrate that launching a constellation as a single unit, with disengagement once in orbit and dispersing using differential drag control, is not only feasible but also scalable.

5. Discussion

This article introduced a novel deployment strategy in which a scalable, many-in-one satellite architecture is launched as a single integrated unit and then dispersed through a staged disengagement sequence combined with differential drag control. While the design of the disengagement mechanism itself remains to be designed, an analytical framework and accompanying algorithms were developed to determine the disengagement timing and velocities for effective in-plane phasing.

The case studies validated this approach under realistic orbital conditions and mission constraints. The simulations confirmed that the algorithm reliably computes phasing times and can accommodate variations in Δv to address operational considerations such as collision avoidance and fault recovery.

The method is notably distinct from established deployment strategies such as those employed by the QB50 mission or Planet Labs [5,16]. Unlike conventional approaches that require post-deployment slot allocation or pre-staged release, the proposed method predefines the full deployment sequence and constellation geometry. This removes the need for slot allocation and instead shifts the control focus to the disengagement velocity and timing, both of which are modeled analytically through simulation.

The deployment of the Planet Labs constellation involves launching multiple individual satellites either simultaneously on a single launch vehicle or across several launches. As a result, the initial condition of the constellation is a dispersed set of satellites in orbit, each with random positions and velocities. To achieve the desired configuration, consisting of n satellites with equiangular spacing around a shared orbital path, each satellite must be assigned a target slot corresponding to one of these equiangular positions and maneuver until the correct phasing is achieved. This process constitutes a stochastic dispersal problem, as both the initial satellite positions and their relative motions are non-deterministic and vary with each deployment. In fact, the system demonstrated by Foster et al. in [5] focuses on optimization algorithms for slot allocation.

The proposed deployment methodology differs from the Planet Labs model in that all satellites are launched as a single, integrated unit. This leads to different initial conditions for the constellation. First, the initial position of all satellites is effectively identical, and the initial relative motion is zero, since they are mechanically connected. Second, the hierarchical disengagement sequence applies controlled changes in velocity at the moment of separation, which governs the initial relative motion instead of leaving it random. Consequently, there is no need for slot allocation after deployment, as each satellite's position is predetermined by its place in the disengagement sequence. Although the same differential drag model is used for subsequent phasing, the underlying problem is different, as it is no longer about slot allocation but instead about selecting disengagement velocity magnitudes and their timing.

The main logistical and economic advantage of this architecture lies in the compact, single-unit launch configuration, which enables high packing efficiency and mass optimization. For example, the PQ8 architecture demonstrated in Case Study 1 can accommodate twice the number of PocketQubes compared to a standard deployer that typically supports four units [19]. However, the extent to which this cost advantage scales with satellite form factor remains to be determined.

The deployment altitude of 500 km at perigee was selected to balance mission lifetime with sufficient atmospheric drag for phasing, also considering its common availability across different rideshare providers. At higher altitudes, drag forces become increasingly negligible, limiting the applicability of passive methods. At lower altitudes, phasing performance improves, but mission lifetime may fall below acceptable thresholds. At the case study altitude, the semi-major axis decay observed during phasing remained negligible, within several kilometers. This should have little impact on mission lifetime, considering that satellites of PocketQube or CubeSat configurations at this altitude would remain in orbit for approximately 5 years.

One of the primary limitations of the approach is the extended phasing duration when the ballistic coefficient ratio is low and no deployables are present. This can be mitigated by increasing the surface area difference between drag modes through additional deployables. However, doing so introduces complexity and potential failure points. Alternatively, relaxing the cube-shaped constraint can improve performance, albeit at the cost of manufacturing and integration complexity. Maintaining both constraints may result in suboptimal phasing durations, and at least one should be reconsidered to ensure mission viability.

Despite this, however, an important advantage of the many-in-one strategy is that satellites can begin operations before final constellation geometry is achieved. This is particularly useful for missions that are not highly sensitive to precise spatial configuration during early operations.

The method also introduces added risk due to the multiple disengagements required. This risk scales with constellation size, as each stage adds a potential point of failure. However, failure at any stage does not necessarily compromise the entire mission, as undeployed units may still operate as part of a reduced-capability constellation. Collision risk is also elevated immediately after separation, as relative velocities are small. This risk is mitigated through careful tuning of Δv, the separation angle, and by leveraging the natural divergence introduced through drag.

Finally, the study relies heavily on simulation and on the NRLMSISE-00 atmospheric model, which has known limitations in capturing fine-scale atmospheric variations [17,20]. While real-time updates to model inputs, such as those applied in Planet Labs' operational systems in [10], can improve accuracy, uncertainties in drag modeling remain a significant challenge in differential drag control.

6. Conclusions

This article introduces a novel deployment method that disengages a many-in-one satellite system into a constellation of smaller satellites. It presents an algorithm that employs differential drag control to determine critical mission parameters, such as disengagement velocities and timings. While real-world validation is still needed, the findings demonstrate a viable approach for managing satellite separation in multi-unit architectures, with potential applications in cost-effective small satellite constellations. It is particularly suited for the following:

(1) Constellations requiring argument of latitude phasing (as demonstrated in the case studies);
(2) Clustered constellations, where clusters of satellites are phased from other clusters, with each cluster consisting of a combination of operational and redundant satellites, providing operational redundancy at each phase;
(3) Short-life space probes: low-cost, lightweight, and disposable satellites for one-time use as space probes;
(4) Interplanetary constellation deployment (for planets with a gaseous atmosphere), where mass and volume budgets are more stringent, and multiple launches are not a feasible option.

Author Contributions: Conceptualization, D.C. and M.A.A.; methodology, D.C.; formal analysis, D.C.; writing—original draft preparation, D.C.; writing—review and editing, M.A.A.; supervision, M.A.A.; project administration, M.A.A.; funding acquisition, M.A.A. and D.C. All authors have read and agreed to the published version of the manuscript.

Funding: The research was partly funded through the projects ASTREA and QUASAR. ASTREA is financed by Xjenza Malta, through FUSION: The R&I technology Development Programme 2019 (R&I-2018-002-T). QUASAR is also funded by Xjenza Malta, through the FUSION R&I: Space Upstream Thematic Programme of 2023 (SUP-2023-02). Additionally, this research was also partly financed by the Ministry for Education, Sport, Youth, Research and Innovation of Malta through the Tertiary Education Scholarship Scheme (TESS) 2021.

Data Availability Statement: The data supporting the conclusions of this article consist of simulations that are graphically reported in the figures. The numerical data from the simulations will be made available by the authors on request.

Conflicts of Interest: The authors declare no conflicts of interest.

Abbreviations

The following abbreviations are used in this manuscript:

ADCS	Attitude Determination and Control System
DM	Disengagement Maneuver
RAAN	Right Ascension of the Ascending Node

Appendix A

In this work, the drag coefficient is computed following the methodology outlined by Moe et al. [18]. Specifically, it is assumed that incident gas particles interacting with the satellite's surfaces undergo re-emission that includes both a diffuse and a quasi-specular component. The diffuse contribution to the drag coefficient, denoted as $c_{D,\ Diffuse}$, is calculated using Sentman's model [21]. The quasi-specular component, $c_{D,\ Specular}$, is derived from Schamberg's quasi-specular accommodation model [22]. The total drag coefficient is then obtained as a weighted sum of these two components:

$$c_D = f c_{D,\ Diffuse} + (1-f) c_{D,\ Specular}$$

where f represents the fraction of interactions resulting in diffuse re-emission, assumed to be 0.9 in this paper for a corresponding altitude of approximately 500 km. This value was selected based on the observations in [23] that the emissions become increasingly specular as the altitude increases. Additionally, at an altitude of 225 km, Space Shuttle data indicate that the factor is approximately 0.98 [24].

The satellite is modeled as a flat plate with a square cross-sectional area. For a gas particle incident at an angle β with respect to the normal surface, Sentman's model provides the diffuse drag coefficient as:

$$c_d A_{ref} = \frac{P}{\sqrt{\pi}} + \gamma Q Z + \frac{\gamma v_r}{2 v_i}\left(\gamma \sqrt{\pi} Z + P\ \right)$$

where $\gamma = \cos(\beta)$, and the intermediate variables are defined as $P = \frac{1}{s} e^{-\gamma^2 s^2}$, $Q = 1 + \frac{1}{2s^2}$, and $Z = 1 + erf(\gamma s)$, with $erf(x) = \int_0^x \exp(-y^2) dy$ and v_i is the incident velocity of the particle with respect to the satellite. Here, s is the speed ratio, representing the ratio of the satellite's speed to the most probable speed of the ambient atmospheric particles. The term v_r denotes the most probable velocity of the re-emitted particle and is given by:

$$v_r = \sqrt{\frac{2}{3}} v_i \left[1 + \alpha\left(\frac{E_w}{Ei} - 1\right)\right]^{\frac{1}{2}}$$

where E_w is the kinetic energy of the remitted molecule with a velocity corresponding to the satellite's surface temperature, and E_i is the average kinetic energy of the incident molecules. The energy accommodation coefficient, α, is calculated using Goodman's formula, as recommended by Moe et al. [25]:

$$\alpha = \frac{3.6\,u\,sin(\beta)}{(1+u)^2}$$

where u represents the ratio of the mass of incoming molecules to that of the surface molecules.

To obtain the quasi-specular component, Schamberg's model is applied to the flat-plate geometry. The specular accommodation, as proposed by Schamberg for a flat plate, is then given by [23]:

$$c_{D,\ Specular} = 2(\,1 - rcos(2\theta))$$

where θ is the incidence angle, and r is the ratio of the satellite's speed to the root-mean-square (rms) speed of ambient atmospheric particles.

Values for the molecule types, average molecular weights of molecules, and atmospheric temperatures were obtained through the NRLMSISE-00 model for the ephemeris data of the satellite. Furthermore, the satellite surfaces are covered in solar cells, and thus, the surface molecular mass is approximated as 60 amu, corresponding to glass [18].

References

1. Crisp, N.; Smith, K.; Hollingsworth, P. Launch and Deployment of Distributed Small Satellite Systems. *Acta Astronaut.* **2015**, *114*, 65–78. [CrossRef]
2. McGrath, C.N.; Macdonald, M. General Perturbation Method for Satellite Constellation Deployment Using Nodal Precession. *J. Guid. Control. Dyn.* **2020**, *43*, 814–824. [CrossRef]
3. Planet Labs PBC. *Planet Imagery Product Specifications*; Planet Labs PBC: San Francisco, CA, USA, 2023.
4. Di Pasquale, G.; Sanjurjo-Rivo, M.; Pérez Grande, D. Optimization of Constellation Deployment Using On-Board Propulsion and Earth Nodal Regression. *Adv. Space Res.* **2022**, *70*, 3281–3300. [CrossRef]
5. Foster, C.; Mason, J.; Vittaldev, V.; Leung, L.; Beukelaers, V.; Stepan, L.; Zimmerman, R. Constellation Phasing with Differential Drag on Planet Labs Satellites. *J. Spacecr. Rocket.* **2017**, *55*, 473–483. [CrossRef]
6. Bussy-Virat, C.D.; Ridley, A.J.; Masher, A.; Nave, K.; Intelisano, M. Assessment of the Differential Drag Maneuver Operations on the CYGNSS Constellation. *IEEE J. Sel. Top. Appl. Earth Obs. Remote Sens.* **2019**, *12*, 7–15. [CrossRef]
7. Gangestad, J.W.; Hardy, B.S.; Hinkley, D.A. Operations, Orbit Determination, and Formation Control of the AeroCube-4 CubeSats. In Proceedings of the Small Satellite Conference, Logan, UT, USA, 10–15 August 2013.
8. Maclay, T.D.; Tuttle, C. Satellite Station Keeping of the ORBCOMM Constellation via Active Control of Atmospheric Drag: Operations, Constraints, and Performance (AAS 05-152). *Adv. Astronaut. Sci.* **2005**, *120*, 763.
9. Jeon, S.; Park, S.Y.; Kim, G.N. Relative Orbit Control Algorithms and Scenarios for the Inertial Alignment Hold Demonstration Mission by CubeSat Formation Flying. *Aerospace* **2024**, *11*, 135. [CrossRef]
10. Sin, E.; Arcak, M.; Packard, A. Small Satellite Constellation Separation Using Linear Programming Based Differential Drag Commands. In Proceedings of the 2018 Annual American Control Conference (ACC), Milwaukee, WI, USA, 27–29 June 2018. [CrossRef]
11. Bakhtiari, M.; Panahyazdan, A.; Abbasali, E. Finite-Time Control for Satellite Formation Reconfiguration and Maintenance in LEO: A Nonlinear Lyapunov-Based SDDRE Approach. *Aerospace* **2025**, *12*, 201. [CrossRef]
12. Falcone, G.; Willis, J.B.; Manchester, Z. Propulsion-Free Cross-Track Control of a LEO Small-Satellite Constellation with Differential Drag. *arXiv* **2023**, arXiv:2306.13844.
13. Ivanov, D.; Monakhova, U.; Guerman, A.; Ovchinnikov, M. Decentralized Control of Nanosatellite Tetrahedral Formation Flying Using Aerodynamic Forces. *Aerospace* **2021**, *8*, 199. [CrossRef]
14. Chernov, K.; Monakhova, U.; Mashtakov, Y.; Biktimirov, S.; Pritykin, D.; Ivanov, D. Decentralized Differential Aerodynamic Control of Microsatellites Formation with Sunlight Reflectors. *Aerospace* **2023**, *10*, 840. [CrossRef]
15. D'Errico, M. Case Study of Along-Track Separation Maintenance of Distributed Synthetic Aperture Radar Systems in Low Earth Orbits. *Aerospace* **2024**, *11*, 600. [CrossRef]
16. Kılıç, Ç.; Scholz, T.; Asma, C. Deployment Strategy Study of QB50 Network of CubeSats. In Proceedings of the 2013 6th International Conference on Recent Advances in Space Technologies (RAST), Istanbul, Turkey, 12–14 June 2013. [CrossRef]

17. Mesalles-Ripoll, P.; Rositani, R.; Duncan, M. Low-Earth Orbit Prediction Accuracy Review of Modern Empirical Atmospheric Models and Space Weather Data Sources. In Proceedings of the Advanced Maui Optical and Space Surveillance (AMOS) Technologies Conference, Maui, HI, USA, 19–22 September 2023.
18. Moe, K.; Moe, M.M. Gas-Surface Interactions and Satellite Drag Coefficients. *Planet. Space Sci.* **2005**, *53*, 793–801. [CrossRef]
19. Twiggs, R.J.; Jernigan, J.G.; Cominsky, L.R.; Malphrus, B.K.; Silverman, B.S.; Zack, K.; McNeil, S.; Roach-Barrett, W. *The PocketQube Concept*; California State Polytechnic University: Pomona, CA, USA, 2014.
20. Akins, K.; Healy, L.; Coffey, S.; Picone, J. Comparison of MSIS and Jacchia Atmospheric Density Models for Orbit Determination and Propagation. *Adv. Astronaut. Sci.* **2003**, *114*, 951–970.
21. Sentman, L.H. *Free Molecule Flow Theory and Its Application to The Determination of Aerodynamic Forces*; Lockheed Missiles & Space Company: Bethesda, MD, USA, 1961.
22. Schamberg, R. *A New Analytic Representation of Surface Interaction for Hyperthermal Free Molecule Flow with Applications to Neutral-Particle Drag Estimates of Satellites*; Rand Corporation: Santa Monica, CA, USA, 1959.
23. Cook, G.E. Satellite Drag Coefficients. *Planet. Space Sci.* **1965**, *13*, 929–946. [CrossRef]
24. Gregory, J.C.; Peters, P.N. A Measurement of the Angular Distribution of 5 EV Atomic Oxygen Scattered off a Solid Surface in Earth Orbit. In Proceedings of the International Symposium on Rarefied Gas Dynamics, Grado, Italy, 16–20 June 1986.
25. Goodman, F.O. Three-Dimensional Hard Spheres Theory of Scattering of Gas Atoms from a Solid Surface I. Limit of Large Incident Speed. *Surf. Sci.* **1967**, *7*, 391–421. [CrossRef]